


RESEARCH ARTICLE

Influence of surface properties on electro-chemical supercapacitors utilizing *Callerya atropurpurea* pod derived porous nanocarbons: Structure property relationship between porous structures to energy storage devices

Vinay S. Bhat^{1,2} | Supriya S¹ | Titilope John Jayeoye³ | Thitima Rujiralai³ | Uraiwan Sirimahachai³ | Kwok Feng Chong⁴ | Gurumurthy Hegde¹ 

¹ Centre for Nano-Materials & Displays (CND), B.M.S. College of Engineering, Bull Temple Road, Bangalore, Karnataka 560019, India

² Department of Materials Science, Mangalore University, Mangalagangothri, Mangalore, Karnataka 574199, India

³ Department of Chemistry and Centre of Excellence for Innovation in Chemistry, Faculty of Science, Prince of Songkla University, Hat Yai, Songkla 90112, Thailand

⁴ Faculty of Industrial Sciences & Technology, Universiti Malaysia Pahang, Kuantan 26300, Malaysia

Correspondence

Gurumurthy Hegde, Centre for Nano-Materials & Displays (CND), B.M.S. College of Engineering, Bull Temple Road, Bangalore 560019, Karnataka, India.
Email: murthyhegde@gmail.com

Abstract

Surface properties always play a dominant role in the energy storage devices. Understanding the surface phenomena is the key to tune the energy storage device using biowaste based porous nano carbons. Here, *Callerya atropurpurea* pod derived peculiar porous nanocarbons are synthesized by pyrolysis at different temperatures without any synthetic templates approach. Elaborate analysis of surface textures on the effect of pore size, volume and specific surface area on specific capacitance and frequency response behavior of nanocarbons were studied in detail. Electrochemical characterizations establish the mutuality of porosity and microtextural properties of nanocarbons with specific capacitance. The electrochemical characterization of the novel materials as supercapacitor electrode shows a high specific capacitance of 326.54 F g⁻¹ at 0.25 A g⁻¹ in 1.0 M KOH. A practical symmetric supercapacitor device is fabricated with a specific capacitance of 86.38 F g⁻¹ at 0.1 A g⁻¹, and high energy density of 27.0 Wh kg⁻¹. This symmetric supercapacitor also possesses outstanding capacitance retention of 92.16% for 5000 charge discharge cycles and also stability of 97.17%, after voltage holding at the maximum voltage for 100 hours. Present manuscript gives the strong evidence for structure-property relationships so that one can tune the energy storage devices effectively.

KEYWORDS

Callerya atropurpurea, nanocarbons, pore size, supercapacitors, surface area

1 | INTRODUCTION

Fossil fuels currently lend lions share to world's energy demand. Natural gas, coal and oil consumption has

significantly risen owing to population boom and global economic proliferation. Global reserves of fossil fuels are depleting fast and their combustion produces greenhouse gases which are detrimental to environment. Hence, the

This is an open access article under the terms of the [Creative Commons Attribution](https://creativecommons.org/licenses/by/4.0/) License, which permits use, distribution and reproduction in any medium, provided the original work is properly cited.

© 2020 The Authors. *Nano Select* published by WILEY-VCH Verlag GmbH & Co. KGaA, Weinheim.

development of green renewable and sustainable source of energy production and conversion technologies are in demand.^[1] Lithium ion batteries, fuel cells and supercapacitors are attractive alternatives to fossil fuels. Supercapacitors differ from batteries in terms of charge storage mechanism. Electrode materials in supercapacitors have very high surface area and porous network which provides for easy diffusion of electrolyte ions and charge storage through electrostatic attraction.^[2] Hybrid electric platforms for trucks, buses and cranes will need storage and delivery of high currents which cannot be accommodated by batteries. Electrochemical capacitors (supercapacitors) can be operated at high galvanostatic process over millions of cycles.^[3,4] Developing such high-performance materials for these devices is the key towards sustainable energy. Carbon is one such material which can be tuned to the requirement and has attracted profound interest. Carbon nanotubes fullerenes, graphene, and other carbon forms have exciting electronic and surface properties which are ideal for energy conversion and storage.^[5] On a flip side, expensive synthetic routes involved in their production, has limited their ability to be used commercially. There is, however, an upside of sorts with 10¹¹ tonnes of carbon generated yearly by biomass production which has been largely untapped for the lack of efficient application in energy storage and conversion devices.^[6]

To produce carbonaceous materials, a carefully designed thermochemical conversion method is needed which can retain and enrich carbon percentage and eject other elements. With careful selection of precursor material and processing conditions such as heating rate, residual plateau, and end temperature, it is possible to form conjugated carbons with sp² state with hierarchical micro-meso pores.^[6-8] Porous nanocarbons can be produced in one pot process unlike templated carbons which require sacrificial template such as nanostructured silica and needs post processing to remove the template. The one pot process is highly acquiescent to industrial scale processing.^[9-11] Significant effort has been done to obtain ideal porous nanocarbon structures for energy storage and conversions.^[12-16] An optimum performance can be expected when porous carbon has high specific surface area (SSA) and well-balanced porosity. Studies have also indicated major role played by micropores influencing the charge and ion storage.^[17] Characterizing the porous nature is primarily important in order to understand the nature of the material used for the energy storage and conversion. Classical BET (Brunauer-Emmett-Teller) and BJH (Barrett, Joyner, and Halenda) models to establish surface area and pore size are though still followed, culminating it with newer methodologies such as, density functional theory (DFT) and non-local density functional

theories (NLDFT) provides a more comprehensive approach to understand the surface nature of the material.^[18]

The present work showcases the influence of pore size and SSA of biomass derived carbon on the performance of supercapacitors in an aqueous electrolyte. Properties of such nano-structured carbons depend on the nature of the carbon precursors.^[10,11,19-24] *Callerya atropurpurea* (CA) pod is used as precursor for synthesis of nanocarbons. The pods are collected from Thailand region and is rich in plant components - cellulose, hemicellulose and lignin.^[6,25] These components when pyrolyzed, undergo different chemical routes to form carbonaceous materials. From earlier reports, it is known that pyrolysis temperature affects the pore size, morphology and micro-textures of biomass derived carbons.^[26] Therefore, to correlate the microtextural properties and their electrochemical behaviour, the biomass was subjected to pyrolysis from 400 to 1000°C. Porosity characters were analyzed and compared by different methods to accommodate for the presence of different types of pores. This method, involving direct pyrolyzed carbon, also demonstrates effectively, a cost-effective green strategy for practical electrochemical energy storage device applications.

2 | RESULTS AND DISCUSSION

The CA pods were carbonized under controlled conditions, in order to obtain porous nanocarbons. A detail investigation had been performed to demonstrate their morphological and surface properties, which would affect electrochemical behaviour. The vital elemental analysis of CA products was conducted by energy dispersive X-ray spectroscopy (EDS) technique.

The result estimated up to 76% of carbon in CA4 and >92% in CA6 to CA10. However, oxygen and nitrogen being essential elements in plant materials were continued to exist in carbonized products in miniature amounts. The EDS plots (Figure S1) also provide evidence about presence of potassium in ~2%. The bar graph, in Figure 1 shows elemental compositions of CA4 to 10; indicating the suitability of higher pyrolysis temperatures. The plot specifically indicates percentage of carbon from CA4 to ≥ CA6 emphasizing higher carbon contents for higher temperatures.

The morphology of carbonized products was studied using field emission scanning electron microscopy (FESEM) and transmission electron microscopy (TEM). The images (Figure 2A, 2C, 2E, 2G and 3A-D) captured by these microscopic techniques corroborated the formation of spherical structures. At higher temperatures, the shape had been defined well and the particles appeared uniformly distributed. Furthermore, the size of these

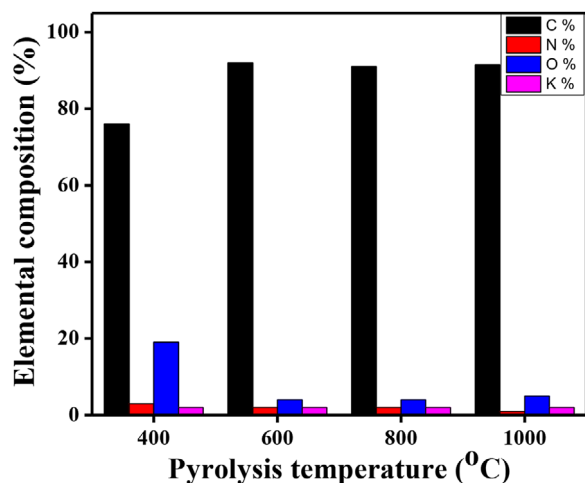


FIGURE 1 Bar graphs showing percentage of different elements present in nanocarbons

carbon structures follows nano-scale; hence, were called nanocarbons. From the Figure 2, particles size decreases as pyrolysis temperature was increased. A wider particle size distribution can be seen (Figure 2B) for CA4 while at higher temperatures, a narrow distribution is observed with majority of the particles obtained with the range of 20–40 nm (Figure 2D, 2F, 2H)

The thermal stability of nanocarbons was tested using TGA method. The percentage mass loss with temperature in inert atmosphere is shown in Figure 4A. TGA was carried out for carbon nanoparticles pyrolyzed at different temperatures. The samples were heated from 25 to 1000°C at 10°C min⁻¹ heating rate. The precursor biomass sample mainly contains cellulose, hemicellulose and lignin. Decomposition of cellulose, hemicellulose and lignin takes place at different temperatures. It was clear from the graph that weight loss in CA4 was maximum, up to 30%; whereas, CA6, CA8, and CA10 materials were comparatively stable with weight loss of 10–12%. CA4 which is synthesized at 400°C, is mainly a pyrolyzed product of hemicelluloses. Pyrolysis of hemicellulose starts around 200°C while that of cellulose begins around 400°C. Hemicellulose is more amorphous with less strength. However, cellulose is more crystalline with long glucose monomer units and is pyrolyzed at higher temperatures than hemicellulose. Lignin, on the other hand, is more cross-linked, making it thermally stable^[27] and decomposition sets in around 700°C. Hence when TGA is performed, the initial mass loss around 100°C is due to the removal of moisture and at higher temperatures, the weight loss observed is due to removal of the residual cellulose and lignin content present in CA4 and CA6. In CA8 and CA10 lignin decomposition would have neared completion during pyrolysis itself and hence exhibit less weight loss.

XRD analysis revealed the formation of amorphous carbon. The broad peaks appeared (Figure 4B) in a range $2\theta = 20$ to 30° and $2\theta = 40$ to 50° , with maximum intensity at 24° and 43° respectively, (ICDD 1071373) were symbolic peaks for carbon. The peaks at these regions indicated arrangement of particles in (002) and (100) lattice planes. The not-so-well defined XRD patterns of CA4 and CA6 hinted the on-going structural transformations, whereas, a sharp peak at $2\theta = 29^\circ$ in CA10, expressed the higher order.

The purity of nanocarbons was also demonstrated by FTIR analysis (Figure 4C). During pyrolysis, heat caused volatile matters to escape from the raw material system. As a result, the carbon matrix was left mainly with carbon and oxygen with negligible amounts of other elements as discussed under EDS section; therefore, corresponding vibrations had been found in the spectra. The peak appeared at 3698 cm^{-1} was attributed to O–H stretching; a stretching vibration of type C=O was found at 2357 cm^{-1} . The peak at $\sim 1589\text{ cm}^{-1}$ was formed due to $\text{C}=\text{C}$ stretching.

Raman spectroscopic analysis showed prominent D and G bands at 1348 cm^{-1} and 1595 cm^{-1} respectively, as shown in Figure S2. A plot of I_d/I_g ratio versus pyrolysis temperature (Figure 4D) manifested increasing intensity of disorder, D band. A similar observation had been reported by Snowdon et. al.,^[28] during the lignin pyrolysis. Another study of nanocarbons derived from waste onion peels by Supriya et. al.,^[26] also showed the increasing disorder which could be attributed to loosely formed particles which break into smaller crystallites, when larger stress was induced in the form of heat.

The chemical nature of nanocarbons, at their surface, was demonstrated by XPS analysis of CA10 material as representation. The wide spectral pattern obtained (Figure 5A) clearly shows two prominent peaks corresponding to carbon (C 1s) at binding energy $\sim 285\text{ eV}$ and oxygen (O 1s) at $\sim 532\text{ eV}$. XPS of C 1s ranging from 280–290 eV (Figure 5B) exhibits six peaks by deconvoluting the C 1s spectrum. The strong main peak at 285 eV could be assigned to the sp^3 carbon atoms (C–C). The other weak peaks centred around 283.8, 285.9, 286.8, and 287.9 eV correspond to C=C, C–O, C–O–C, and C=O groups respectively,^[29] originating from the groups in the intermediate small molecules which are retained at the edges and defects in the nanocarbons.^[30] The deconvolution of O 1s spectrum yields four subpeaks centred at 531, 532.3, 533.6, and 534.9 eV (Figure 5C) which could be ascribed to different oxygen functionalities such as C=O, C–O, O=C–O, and O–H respectively.^[31,32] As the composition of nitrogen present was less, XPS of N 1s did not yield sufficient information and the spectrum is provided in Figure S3.

The XRD, Raman spectroscopy and XPS analyses hint at the development of disordered nanocarbons from CA.

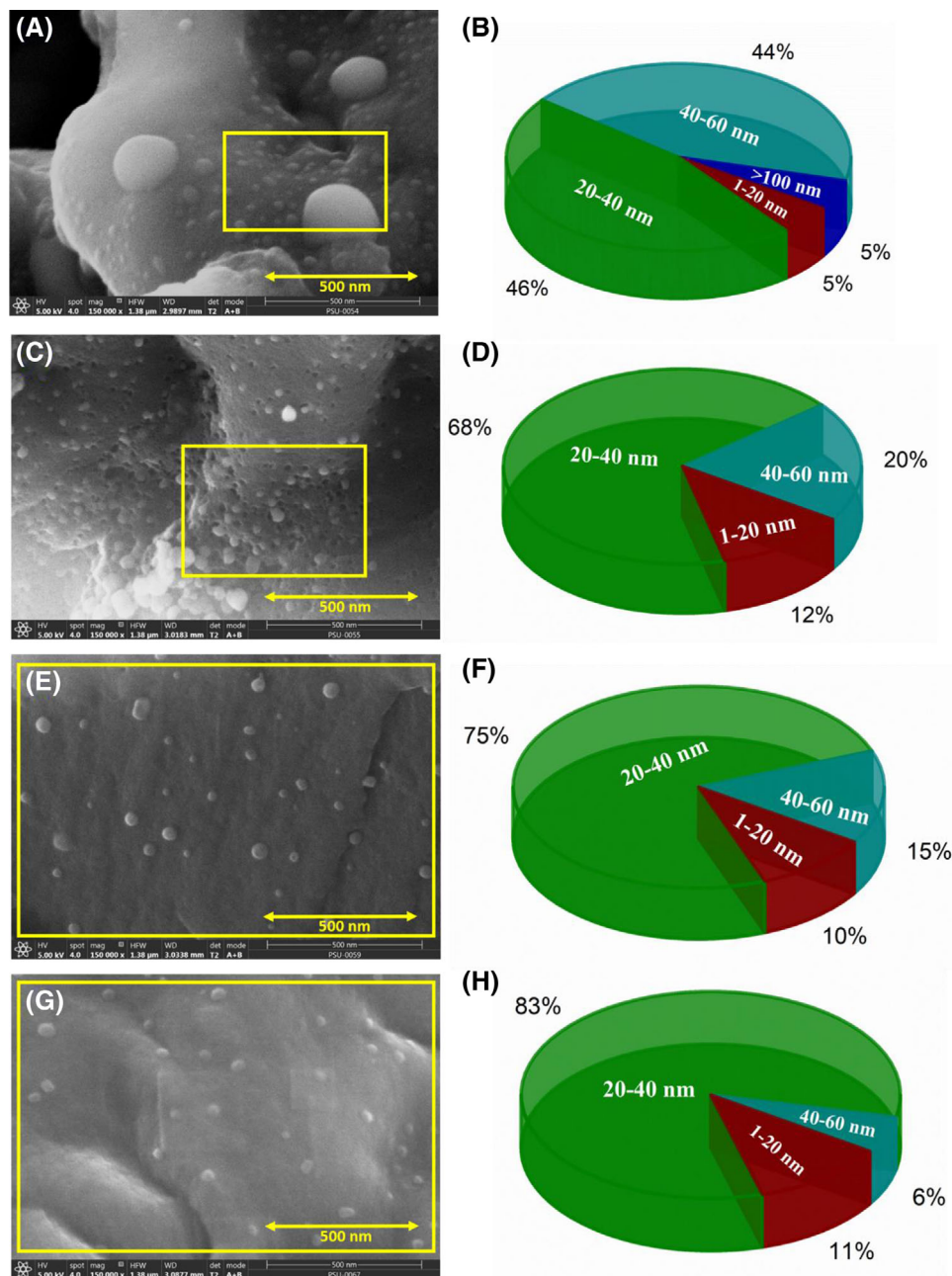


FIGURE 2 FESEM images of carbonized materials showing spherical morphology, (A) CA4 (C) CA6 (E) CA8, and (G) CA10. Marked area was used to count the particle size distribution with decrease in particle size as pyrolysis temperature is increased and is represented in a pie chart for (B) CA4, (D) CA6, (F) CA8, and (H) CA10.

The formation of amorphous carbon has been identified by the broad peaks in the XRD patterns. The same has been corroborated by higher D band intensity in Raman spectra. Further XPS analysis also indicated the presence of greater quantity of sp^3 carbon atoms (C—C). Hence, the material characterizations confirm the formation of disordered carbon particles with some degree of graphitization (G band in Raman spectra).

A detailed investigation had been performed to demonstrate the surface properties of CA pods derived nanocarbons. Surface area of CA nanocarbons were obtained from

N_2 adsorption desorption isotherm experiment carried out at 77 K (Figure 6). CA4 and CA6 exhibit type IV H_2 isotherm which are typical of disordered materials with not well-defined pore size and shapes. CA8 shows type IV with a large rise in the amount of N_2 adsorbed at low relative pressure ($p/p_0 < 0.2$) and a hysteresis loop at $0.2 < p/p_0 < 1.0$ indicate presence of mesopores.^[33,34] CA8 and CA10 predominantly exhibit H_4 isotherm of materials with narrow slit pores including pores in micropore region.

Accuracy was confirmed by performing both single point and multipoint methods; the two methods confirmed

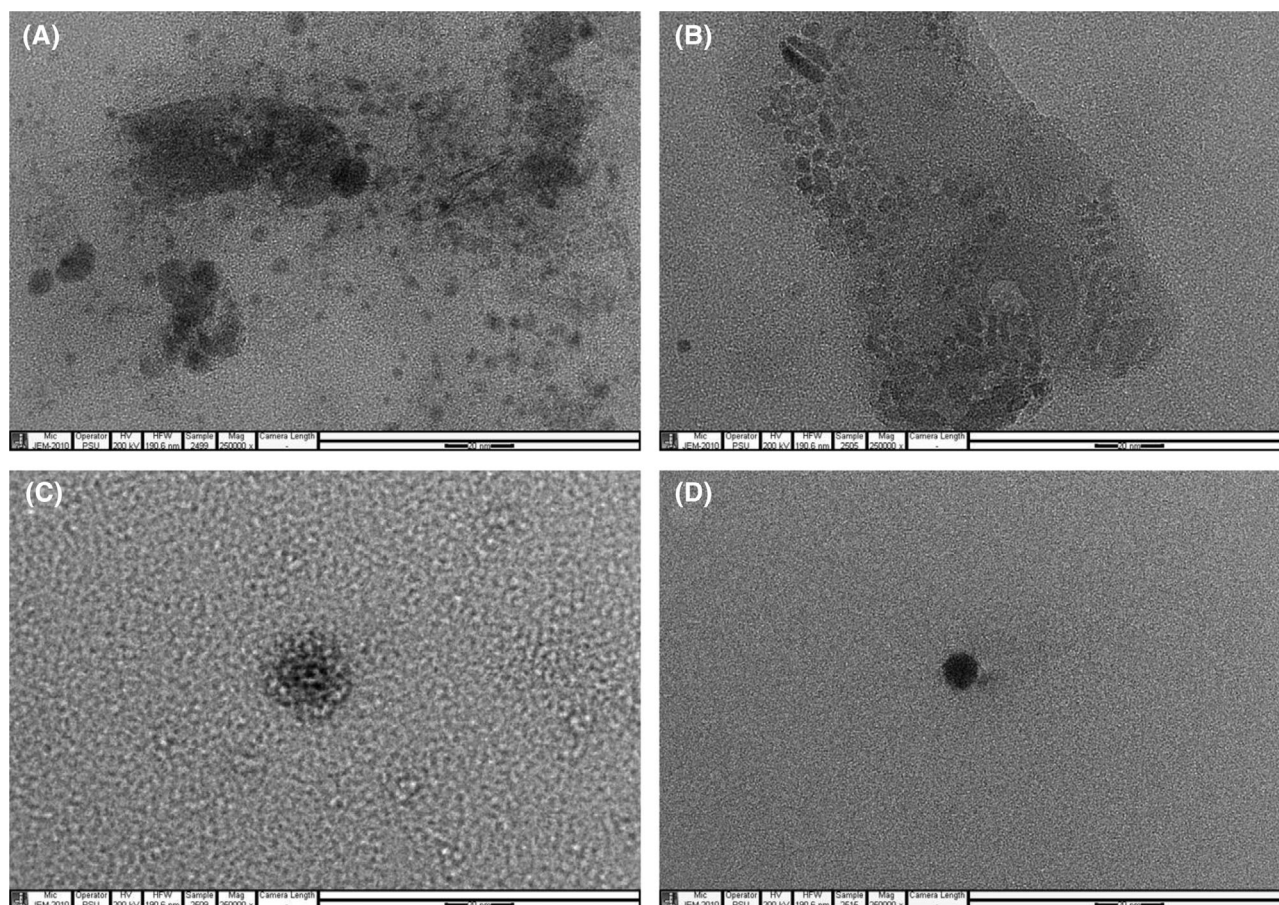


FIGURE 3 TEM images of carbonized materials, (A) CA4, (B) CA6, (C) CA8, and (D) CA10

highest value for CA8, $991 \text{ m}^2 \text{ g}^{-1}$, and $1241 \text{ m}^2 \text{ g}^{-1}$, respectively (Table 1). The Figure S4a represents BET surface area values of CA materials by single and multipoint methods. Various methods were employed to determine the porosity of nanocarbons. The techniques helped to correlate effect of porosity on electrochemical behaviour of nanocarbons by surveying surface area of pores, pore width and pore volume. The studies carried out using BJH, Dollimore-Heal (D-H), t-plot, Dubinin-Astakhov (DA), Micropore analysis (MP), DFT and NLDFT methods. The summary of results obtained for every study are given in Tables 1–3.

BJH and D-H methods were employed to analyze larger pores ($\geq 1.5 \text{ nm}$).^[35] The pore size distribution curves (Figure 7) obtained from BJH method indicates higher pore volume for pores having size $\sim 1.5\text{--}2.0 \text{ nm}$. This represents the presence of a combination of micropores and mesopores in the nanocarbons. The surface area of pores determined by these methods were corroborating with exhibiting BET. The highest value for nanocarbons formed by pyrolyzing the pods at 800°C (2363 and $111 \text{ m}^2 \text{ g}^{-1}$, respectively, as shown in Figure S4b). Further, other methods such as t-plot, DA, and MP were employed to

determine surface area of micropores; the largest values were obtained for CA8 and are as follows, 1230 , 1435 , and $1490 \text{ m}^2 \text{ g}^{-1}$ respectively.

The above methods were also used to determine average pore width of CA nanocarbons samples (Table 2). BET and BJH methods showed similar trend and they showed the pore size in micropore region ($< 2 \text{ nm}$), where average pore width decreased from CA4 to CA10, as seen in Figure S5a. The D-H was used to analyse the pores having size $> 1.5 \text{ nm}$,^[35] below which the method was not effective for cylindrical pores. The pore width analysis conducted by D-H method followed zig-zag like trend, where, CA4 and CA8 had the low values, once again CA8 exhibiting the lowest and CA6 and CA10 exhibited higher values.

An investigation on the amount of micropore volume in CA derived nanocarbons was conducted by various methods such as BJH, t-plot, MP, DA, and Horvath-Kawazoe (HK) method. The results obtained by the mentioned methods are given in Table 3. The corresponding plots obtained are given in Figure S5b. The BJH, t-plot, HK, and DA methods showed the highest values for CA8 nanocarbons, 0.63 , 0.07 , 0.49 , and $0.60 \text{ cm}^3 \text{ g}^{-1}$, respectively. MP

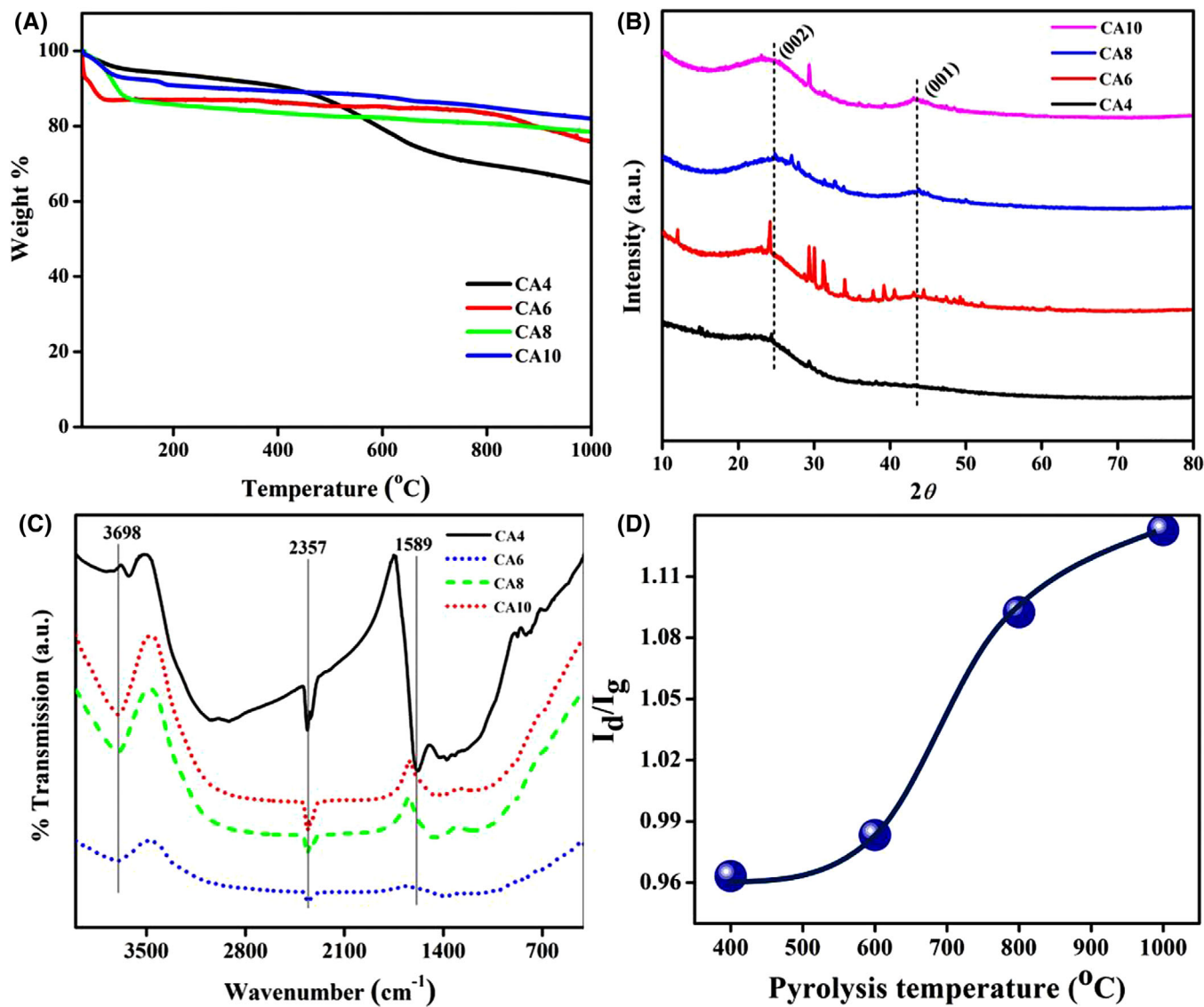


FIGURE 4 (A) TGA plots, (B) XRD patterns, and (C) FTIR spectra of CA4, CA6, CA8, and CA10. (D) Plot showing increasing I_d/I_g ratio with pyrolysis temperature obtained from Raman spectroscopic analysis.

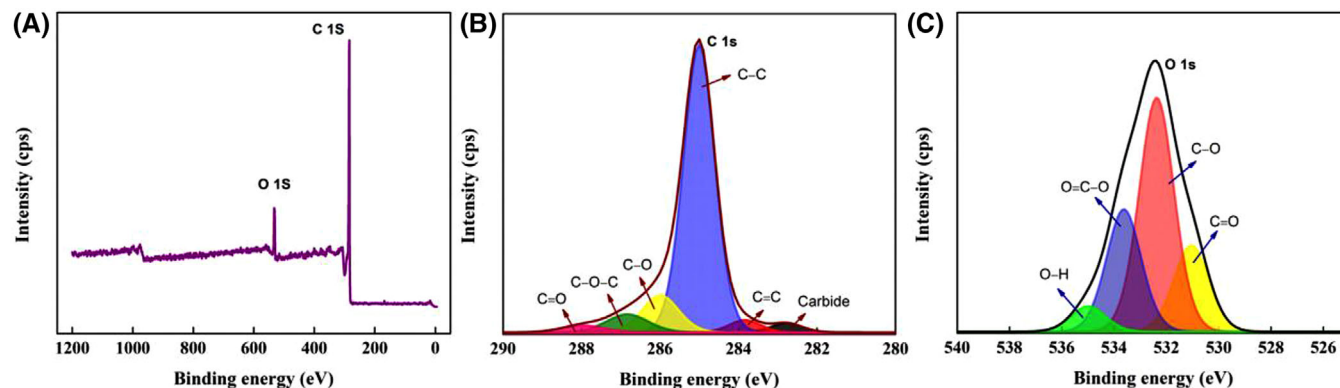


FIGURE 5 Convolved XPS spectrum of CA10 (A) Deconvoluted C 1s spectrum (B) and O 1s spectrum (C).

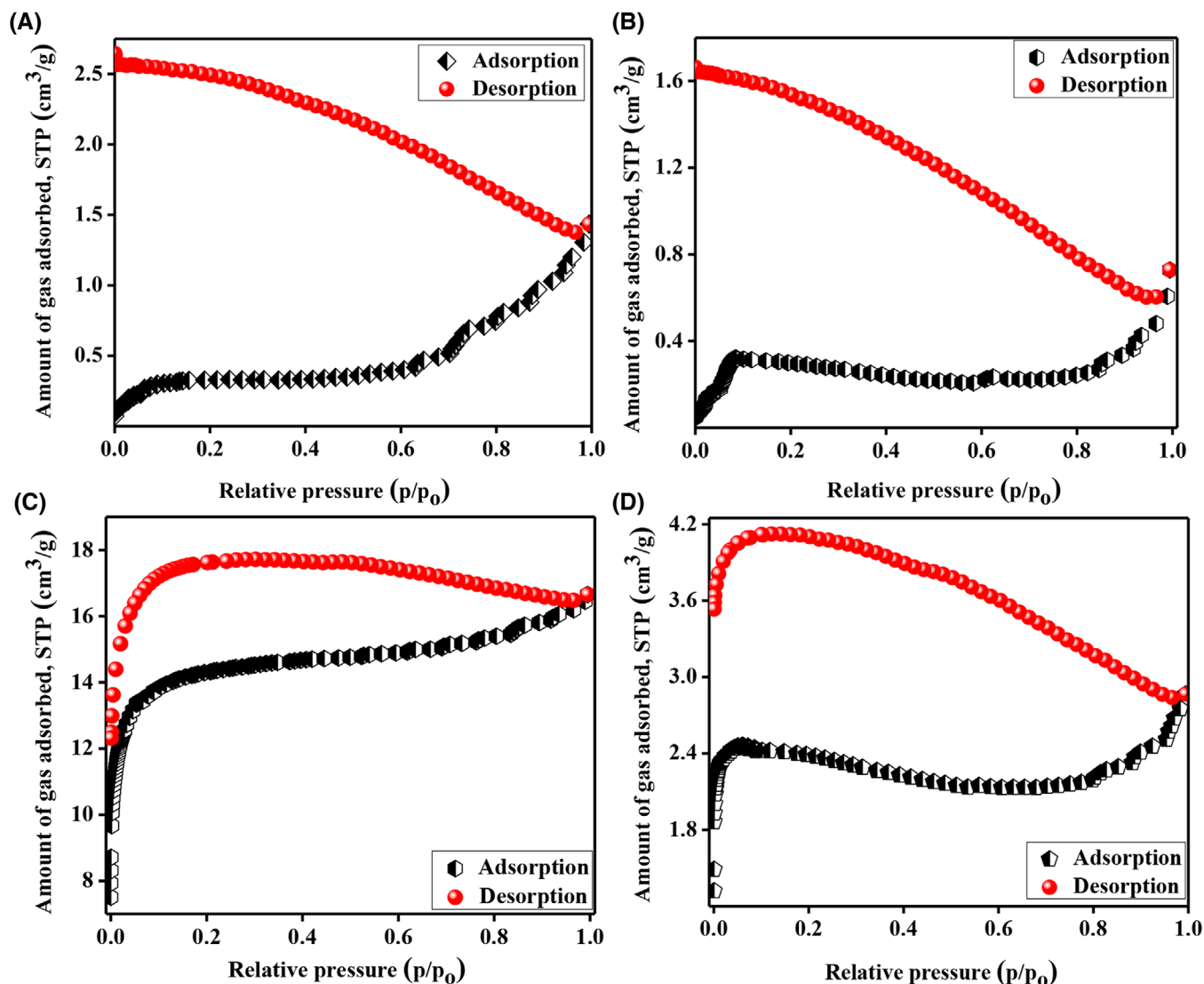


FIGURE 6 N_2 adsorption-desorption isotherms of CA4 (A), CA6 (B), CA8 (C), and CA10 (D)

TABLE 1 BET surface area of CAs and surface area of pores as calculated by various methods

Material	Single point surface area ($m^2 g^{-1}$)	BET surface area ($m^2 g^{-1}$)	BJH surface area of pores ($m^2 g^{-1}$)	D-H surface area of pores ($m^2 g^{-1}$)	External surface area t-plot ($m^2 g^{-1}$)	DA micropore surface area ($m^2 g^{-1}$)	MP surface area of pores ($m^2 g^{-1}$)	DFT area in pores ($m^2 g^{-1}$)	NLDFT area in pores ($m^2 g^{-1}$)
CA4	23	27	47	17	26	25	5	14	11
CA6	19	31	52	3	100	20	23	9	5
CA8	991	1241	2363	111	1230	1435	1490	299	210
CA10	159	227	168	5	96	212	321	29	1

method was basically an extension of t-plot method to analyze narrow pores;^[36] the methods evidenced large micropore volume of CA8 nanocarbons quantified as 0.57 and $0.07 \text{ cm}^3 \text{ g}^{-1}$, respectively in comparison with CA4, CA6, and CA10.

Total pore volume and surface area of nanocarbons were calculated using DFT and NLDFT techniques. As in previous studies, here also CA8 material had shown highest value (Figure S6a and S6b) in comparison with CA4, CA6, and CA10, evidenced that

TABLE 2 Pore width of CAs calculated from different methods

Material	BET average pore width (nm)	BJH average pore width (nm)	D-H average pore width (nm)	HK median pore width (nm)	MP average pore hydraulic radius (nm)
CA4	7	4	11	1	1
CA6	3	2	25	1	<1
CA8	2	1	5	0.5	<1
CA10	2	1	23	0.5	<1

TABLE 3 Pore volume of CAs calculated from various methods

Material	Single point pore volume ($\text{cm}^3 \text{g}^{-1}$)	BJH pore volume ($\text{cm}^3 \text{g}^{-1}$)	t-plot pore volume ($\text{cm}^3 \text{g}^{-1}$)	HK pore volume ($\text{cm}^3 \text{g}^{-1}$)	DA micropore volume ($\text{cm}^3 \text{g}^{-1}$)	MP pore volume ($\text{cm}^3 \text{g}^{-1}$)	DFT total pore volume ($\text{cm}^3 \text{g}^{-1}$)	NLDFT total pore volume ($\text{cm}^3 \text{g}^{-1}$)
CA4	0.05	0.05	0.00	0.01	0.01	0.00	0.05	0.00
CA6	0.02	0.02	0.00	0.01	0.01	0.00	0.02	0.02
CA8	0.57	0.63	0.07	0.49	0.60	0.57	0.48	0.53
CA10	0.10	0.05	0.05	0.08	0.08	0.10	0.08	0.09

CA8 possesses excellent surface features like area and porosity.

During pyrolysis, abundant reactive gaseous species are generated. Such species are expected to create considerable nanopores.^[37] For CA4, CA6, and CA8, the BET SSA increases due to increased degree of decomposition. Above 800°C, the increase of pyrolysis temperature might lead to collapse of porous structures; micropores formed in the early stage or the combination of micropores into mesopores and macropores which invariably decreases the SSA.^[38] The porosity results obtained from various methods indicate that multipoint BET method is still the most useful to obtain the SSA. Methods based on the Kelvin equation (e.g., BJH-method) are linked to the pore condensation phenomena, that is, they are mostly suitable for mesopore size analysis. Other classical theories, like for instance the Dubinin-Radushkevich approach, and semiempirical treatments such as those of Horvath and Kawazoe (HK), are dedicated to describe micropore filling. Hence, in cases when a material contains both, micro- and mesopores, at least two different methods have to be used to obtain the pore size distribution(s) from such an adsorption/ desorption isotherm. In addition, the accuracy of such thermodynamic, macroscopic methods is limited, because of the assumption that the pore fluid has similar thermophysical properties as the bulk fluid. In contrast to these macroscopic approaches, methods like the DFT provide microscopic model of adsorption and also a more realistic description of the thermodynamic properties of the pore fluid. These theories, which are based on statistical mechanics, connect macroscopic properties to the molecular behavior.^[18] However, all the methods used to

obtain SSA, pore size distribution and porosity exhibit the similar trends.

To evaluate the electrochemical performances of nanocarbons, cyclic voltammetric (CV) experiments were conducted in a three-electrode setup using 1.0 M KOH as the electrolyte. The fabricated electrodes were operated at potential window of -1.0 to 0 V. CV plots (Figure S7) exhibited absence of faradic charge transfer. It is evident from the plot that the shape of the I-V curve becomes rectangular as the pyrolysis temperature increases, indicating a decreased equivalent series resistance with increase in pyrolysis temperature. A very minor hump like feature is exhibited at low scan rate of 10 mV s^{-1} , could be due to pseudo capacitance contribution from heteroatoms such as O, N in CA materials (Figure S1 and S7). However, as the scan rate is increased, the current response is also amplified; thereby, the effect of pseudo capacitance is completely absent. The CV curves of CA4 (Figure S7a) shows distorted non rectangular loop even at low scan rate of 10 mV s^{-1} . The current density observed for applied potential was less indicating CA4 to be not a good capacitive material. This can be explained on the basis of lesser carbon percentage, and lesser surface area and not well-developed porous structures for CA4 as reported in earlier sections. From CA6 onwards all materials exhibited quasi-rectangular shapes, which are typical of an electrochemical double layer capacitor (EDLC). Among them CA8 (Figure S7c) retained rectangular shape even at higher scan rates. Since, CA4 didn't exhibit desirable characteristics as seen from its CV (Figure S7a), further electrochemical investigations were carried out with CA6, CA8, and CA10 only.

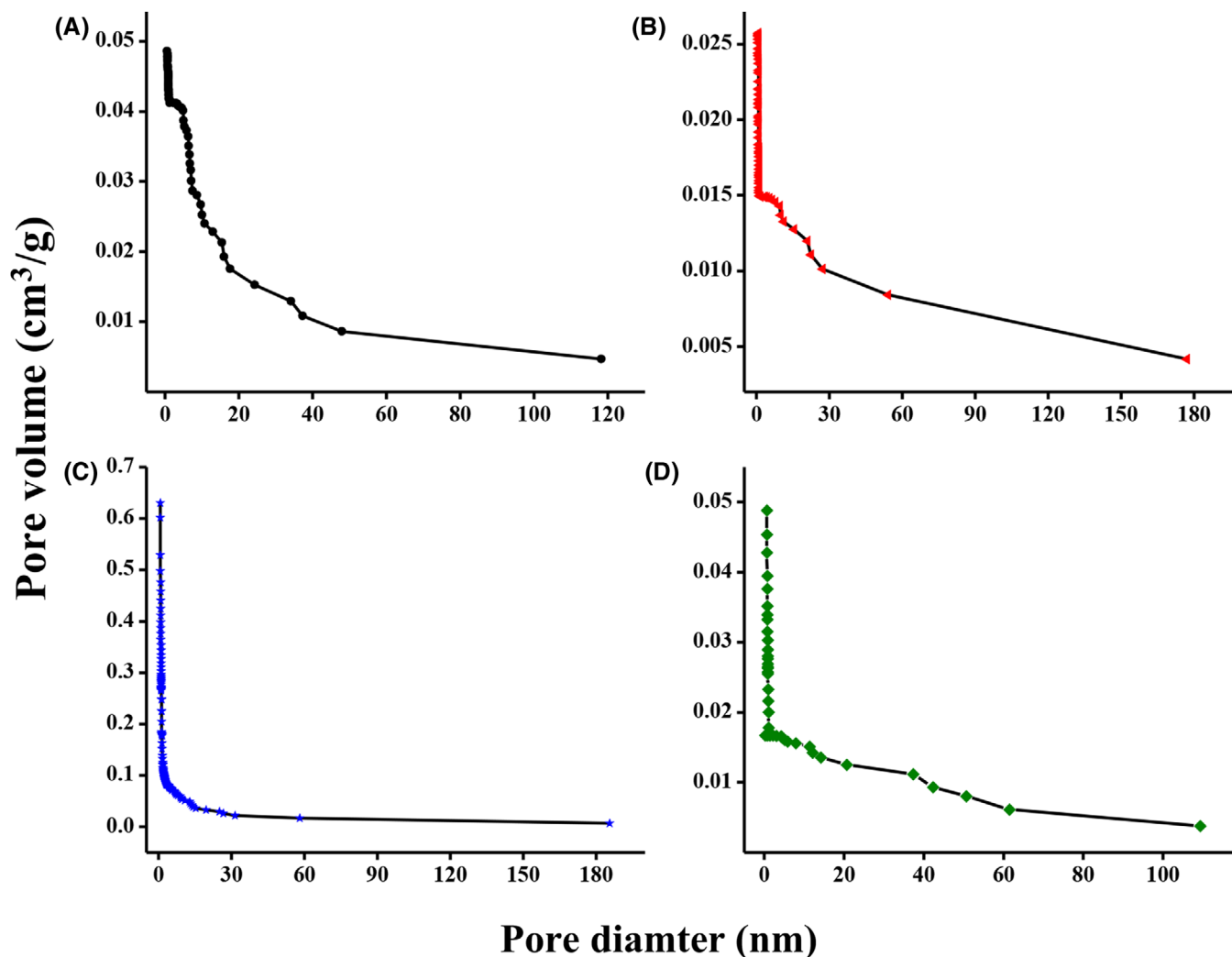


FIGURE 7 Pore size distribution curves obtained for nanocarbons CA4 (A), CA6 (B), CA8 (C), and CA10 (D) from BJH studies

The constant current galvanostatic charge discharge curves for three electrode system in 1.0 M KOH is depicted in Figure S8. The plots are fairly linear and symmetrically triangular which indicate rapid electrolyte diffusion mechanism leading to a faster I-V response. A slightly non-linear galvanostatic discharge profiles (Figure S8b-d) at lower current density (0.25 A g^{-1}) suggests contribution of pseudo capacitance. This is in agreement with minor humps observed at lower scan rate in CV studies. Specific capacitance was calculated from charge-discharge profiles using the following equation;^[39]

$$C_{\text{sp}} = \frac{I \times \Delta t}{\Delta V \times m} \quad (1)$$

where, I and Δt being discharge current and discharge time (s) respectively; ΔV represents the operating potential window (V) while the mass of the CA nanocarbons active material loaded onto the electrode is repre-

sented by m . The galvanostatic charge discharge profiles (Figure S8d and S8e) at 0.25 A g^{-1} further confirms that electrode CA8 exhibits higher capacitance than CA6 and CA10. CA8 electrode exhibited specific capacitance of 326.74, 180.77, 139.60, 130.07 F g^{-1} from the charge discharge profiles at current density of 0.25, 0.5, 0.75, and 1.0 A g^{-1} respectively. Typically, the micro and mesoporous surfaces impart high surface area, which will enhance diffusion of electrolyte thereby increasing specific capacitance and energy density of the supercapacitor.^[40] Specific capacitance is increased remarkably at low charging rate (low current density) as the electrolyte will diffuse through entire micro and mesopores. However, at high charging rates the electrolyte can access only the larger pores which will diminish the specific capacitance. The surface area studies by various methods suggests presence of hierarchical micropores and mesopores. From Figure S8e, it is apparent that, maximum specific

TABLE 4 Fitting parameters of the experimental impedance data at OCP for CAs in 1.0 M KOH

Material	R_s (Ω)	R_{CT} (Ω)	C (mF)	CPE (mF)	W (Ω)
CA6	1.04	2.249	142	1.08	1.9
CA8	0.4	0.407	785	34.1	0.41
CA10	0.98	1.79	398	15.1	0.552
CA8 cell ^a	0.937	0.211	359	33	0.236
CA8 cell ^b	1.29	0.438	157	29.9	0.201

^aBefore 5000 cycles.^bAfter 5000 cycles.

capacitance is achieved for CA8. Above 800°C, the gravimetric specific capacitance was decreased (as also the surface area). Porous surface area calculated from BET, BJH, DFT, and NLDFT (Table 1) point towards a higher surface area for CA8. Specific capacitance as a function of current density is shown in Figure S8e. At high current density initial specific capacitance retention of 41% was attained, indicating good rate capability of CA8 electrodes for supercapacitor applications.

To analyse frequency response behaviour of nanocarbons, EIS (electrochemical impedance spectroscopy) was conducted. Figure S9a shows the Nyquist impedance plots of CA materials measured at a frequency range of 0.01 to 10⁵ Hz with an amplitude of 5 mV. The plot depicts the typical features of porous nanocarbon electrodes, with a 45° Warburg region at lower frequency and a semicircle at high frequency. The length of the 45° region corresponds to Warburg impedance caused by the ion diffusion from the bulk of electrolyte into the electrode interface.^[41] The intercept on the X-axis indicated by R_s which represents the combined resistance of the ions in electrolyte, inherent resistance of the active electrode material and contact resistance with the current collector. R_s value in the range of 1.05–0.4 Ω was obtained, with 1.06 Ω for CA6 and 0.4 Ω for CA8 indicating a very low resistance and good ion response at high frequency region. Further, the diameter of the semicircle is the charge transfer resistance (R_{CT}),^[14] also shows a significant decrease from 2.25 Ω for CA6 to 0.407 Ω for CA8. Key parameters obtained after fitting with the data are tabulated in Table 4. Applied frequency affecting the phase angle is shown in Figure S9b. The frequency at which phase angle reaches 45°, is where the capacitive and resistive impedances are equal. At higher frequencies supercapacitors show resistive nature.^[42] Relaxation time constant (τ_0) is an indicator of responsiveness of the supercapacitors which is the reciprocal of characteristic frequency representing a quantitative measure of how quickly the system can be charged and discharged. It was calculated from pre-formulated equations.^[2,43] τ_0 calculated for CA6, CA8, and CA10 was found to be 1.59, 0.44,

and 1.22 seconds respectively, which is in agreement with the results from CV and charge discharge profiles. Also, from bode plot (Figure S9b) it is clear that, CA8 in 1.0 M KOH, with phase angle -72.05° is quite comparable to an ideal capacitor (-90°).^[44] Figure S9c exhibits the evolution of C' normalized by C'_{\max} (0.01 Hz) against frequency calculated according to equation 2 and 3. As frequency is a dependant variable, this is a better way to represent the frequency response as Nyquist plot has frequency buried in impedance terms. The plot represents transition between resistive behaviour at C'/C'_{\max} equal to zero to capacitive behaviour at C'/C'_{\max} equal to 1. Capacitance was found to be increasing with decreasing frequency. Figure S9d represents the unfolding of the imaginary part of capacitance (C'') with frequency.

$$C' = \frac{-Z''}{\omega(Z)^2} \quad (2)$$

$$C'' = \frac{-Z'}{\omega(Z)^2} \quad (3)$$

where, C' and C'' represents the real and imaginary capacitances, Z'' is imaginary part of the complex impedance, $\omega = 2\pi f$, Z is the overall complex impedance. C' , calculated at the lowest applied frequency attributes to the energy stored in supercapacitors.^[2]

Vix-Guterl et al.^[10] and J. Chmiola et al.^[45–47] in their pioneering works, demonstrated using synthetic carbon sources with templates and metal carbides that, the decrease of specific capacitance with increase in pore size and synthesis temperature even when the surface area was increasing. In this context, in the present work, the surface area and pore size decreased with increase in temperature. Decrease of surface area above 800 °C could be due to multiwalled graphitic carbon formation. Due to small interplanar spacings, the area between the walls may not have been accessible to N_2 .^[45] For the same reason, electrolyte ions may not be able to access entire surface and resulting in decrease of specific capacitance for CA10, synthesized at 1000 °C (Figure 8A). The above results show that porosity and SSA growth follows same trend as supported with XRD and Raman. After 800°C the gravimetric specific capacitance decreased correlating well with decreased surface area (both BET and DFT) (Figure 8A,B). The specific capacitance also exhibited a decreasing trend with increasing average pore width (Figure 8C). This can be explained by considering the ultramicropores ($d < 0.7$ nm) which are believed to harbour non-solvated electrolyte ions which account for bulk of double layer capacitance.^[10,46] BJH and DH pore distribution methods based on Kelvin equation and capillary condensation phenomenon are questionable for small corral of micropores. HK (Horvath and

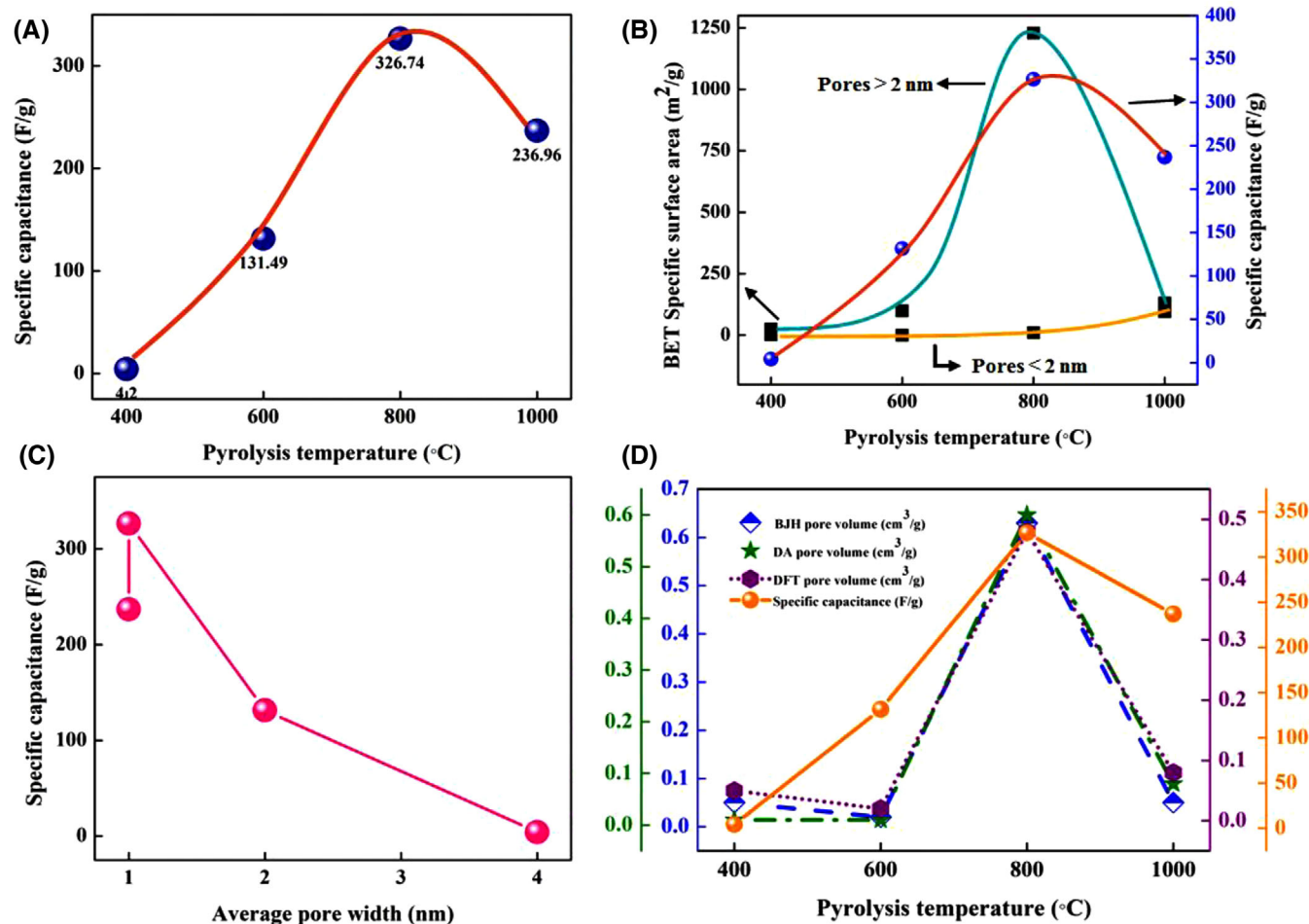


FIGURE 8 (A) Specific capacitance with pyrolysis temperature shows a maximum at 800°C. (B) Mesopore (>2 nm) and micropore (<2 nm) surface area in comparison with specific capacitance for CA. (C) Specific capacitance with average pore size exhibiting a decreasing trend with increasing pore width above 1 nm. (D) Multiple pore volume models in comparison with specific capacitance. A direct relation between pore volume and specific capacitance is observed.

Kawazoe) method, manifests a pore size distribution in the micropore range^[48] on differentiation of volume of gas adsorbed relative to the total uptake, with respect to the effective pore width which predominantly is for slit like micropores. Presence of such ultramicropores is confirmed from Table 2, with pore width of 0.5 nm for CA8. A striking feature observed (Figure 8B) for CA8, is the presence of large mesoporous surface area of 1229.81 m² g⁻¹ (Table 1) as obtained from DH and BJH models. This is quite peculiar as pore width for CA establishes it to be a micropore. This also suggests formation of highly ordered hierarchically porous carbons during pyrolysis. Also, with increase in temperature, the increased surface area is due to mesopores at the expense of micropores.^[45] Shi^[49] presented a simple model which sums up micropore and mesopore contribution to capacitance into two components. Pores size more than 2 nm have one fixed specific surface capacitance (C_{meso}) and pores smaller than 2 nm have another

(C_{micro}). The total specific capacitance is as shown in equation (4);^[45]

$$C = S_{\text{meso}} C_{\text{meso}} + S_{\text{micro}} C_{\text{micro}} \quad (4)$$

Where, S_{micro} and S_{meso} are the surface contributions from pores larger than 2 nm and smaller than 2 nm respectively. The results indicate that, not just the pore size and surface area but also the contortion in pores matters. It is believed that, for electrochemical applications, bimodal porosity having micropores and meso/macro pores are ideal due to the energy storage occurring predominately in the smaller micropores while the larger pores provide fast mass-transport of electrolytes back and forth the micropores.^[10,25,46] Figure 9 schematically illustrates such bimodal pores and charge (ion) storage with solvated ions and non-solvated ions residing in mesopores and micropores respectively.

FIGURE 9 Schematic illustration of solvated ions and non-solvated ions residing in mesopores and micropores respectively.

Porous nanocarbons

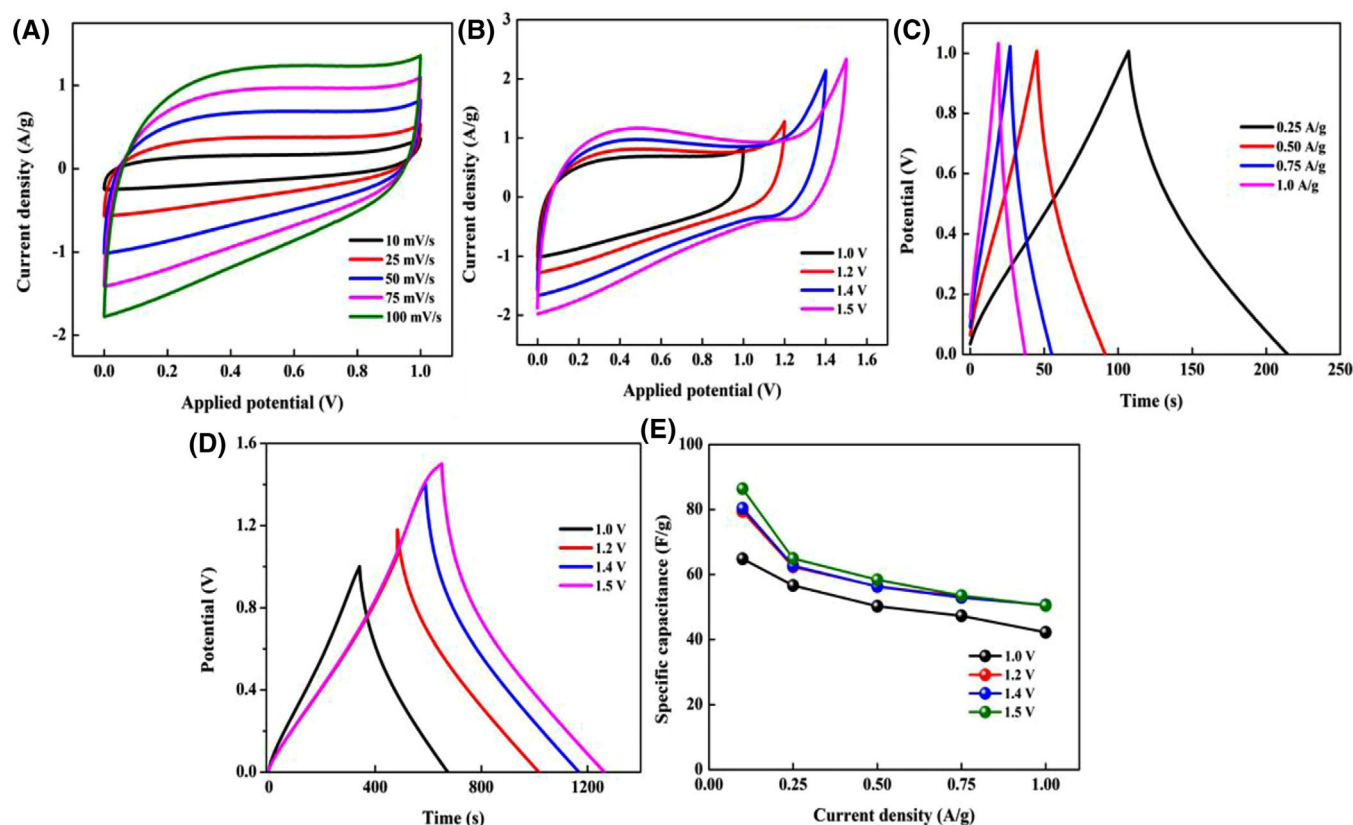
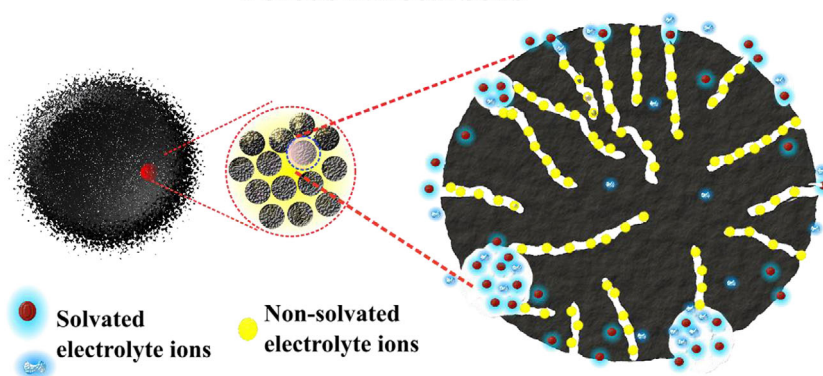


FIGURE 10 CV plot of CA8 symmetric supercapacitor at different scan rates (A), CV at different potential window at 50 mV s⁻¹ (B), constant current charge/discharge curves at different current densities (C), constant current charge/discharge curves at different potential window under current density of 0.25 A g⁻¹ (D), plot of variation of specific capacitance with current density for CA cell under different potential windows (E).

2.1 | Electrochemical measurements of practical symmetrical supercapacitor

The effect of porosity of CA8 material on device performance was studied by fabricating a CR2032 symmetrical supercapacitor coin cell. Figure 10A shows the CV plot of cell with a potential window of 1.0 V. The CV curves show rectangular shape at lower scan rates and

the profile is retained to a larger extent even at higher scan rates. Oxidation-reduction peak was not observed, indicating pure capacitive behaviour of the fabricated device. Absence of any characteristic redox peaks while, potential window was increased from 1.0 to 1.5 V (Figure 10B), indicates capacitive behaviour and signifies the capability of CA8 device for operating at higher potential windows. Charge/discharge curves at different

TABLE 5 Key energy performance indicators of CA8 symmetric supercapacitor

Symmetric supercapacitor	Potential (V)	Current density (A g^{-1})	Specific capacitance (F g^{-1})	Energy density (Wh kg^{-1})	Power density (W kg^{-1})
CA8	1.0	0.1	68.84	9.00	97.65
		1.0	42.19	5.85	1171.94
	1.2	0.1	79.43	15.88	107.10
		1.0	50.49	10.09	1398.21
	1.4	0.1	80.38	21.88	136.29
		1.0	50.65	13.78	1654.62
	1.5	0.1	86.38	27.0	158.79
		1.0	50.45	15.76	1773.63

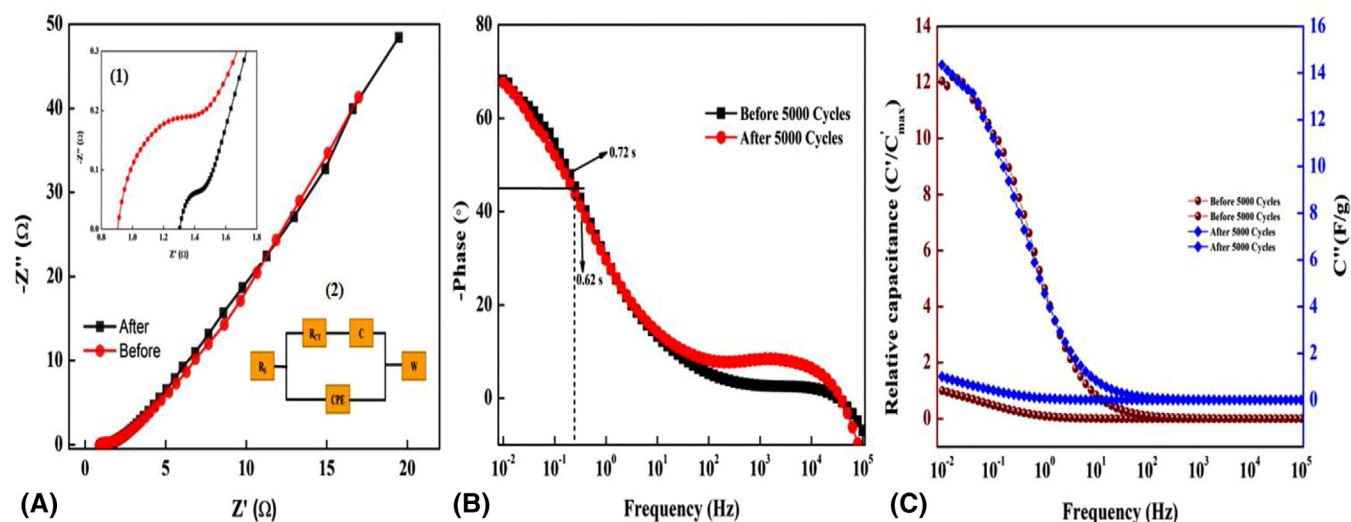


FIGURE 11 Nyquist impedance plot of CA8 symmetrical supercapacitor (A), before and after 5000 charge-discharge cycles. The inset(1) shows the zoomed view of Nyquist impedance of (A) at high frequency region showing semicircle and an equivalent circuit is depicted in inset (2), Bode phase angle plot as a function of frequency (B), Relative real capacitance (C') and imaginary (C'') part of the capacitance as a function of frequency before and after 5000 charge discharge cycles (C)

current densities from 0.1 to 1.0 A g^{-1} under different potential windows (Figure 10C,D) displayed triangular, linear symmetrical nature with bare minimum iR drop, confirming the EDLC behaviour and good electrochemical reversibility of the CA8 cell. In three electrode setup, complete potential window is applied on the working electrode wherein for symmetrical supercapacitor device/cell, the applied potential is shared between the two electrodes.^[50] For the same reason, the capacitances are lower than that obtained for CA8 in three electrodes set up (326.74 F g^{-1}). The fabricated supercapacitor cell had a C_{sp} of, 86.38 F g^{-1} , 80.38 F g^{-1} , 79.43 F g^{-1} and 64.8 F g^{-1} at 1.5, 1.4, 1.2, and 1.0 V operating potential at 0.1 A g^{-1} respectively. Variation specific capacitances with current density is plotted in Figure 10E and key energy performance are listed in Table 5.

Electrochemical impedance measurements revealed the impedance behaviour of the device. The device exhibited very low charge transfer resistance of 0.212Ω . (Table 4). The Nyquist impedance plot with low R_s value of 0.937Ω with high electrical conductivity is exhibited by the device as suggested by the EIS results (Figure 11A). An appropriate equivalent circuit model (Inset 2 Figure 11A) was fitted. With Ionic diffusion is represented by a vertical line at lower frequencies characterized by Warburg impedance at -45° phase angle.

The Bode plot (Figure 11B) shows the phase angle of -68.25° . τ_0 for the fabricated device, at characteristic frequency was found to be 0.62 seconds. Real and imaginary capacitance are also plotted against frequency (Figure 11C). The capacitances remain nearly invariant with frequency indicating ideal nature of fabricated device.

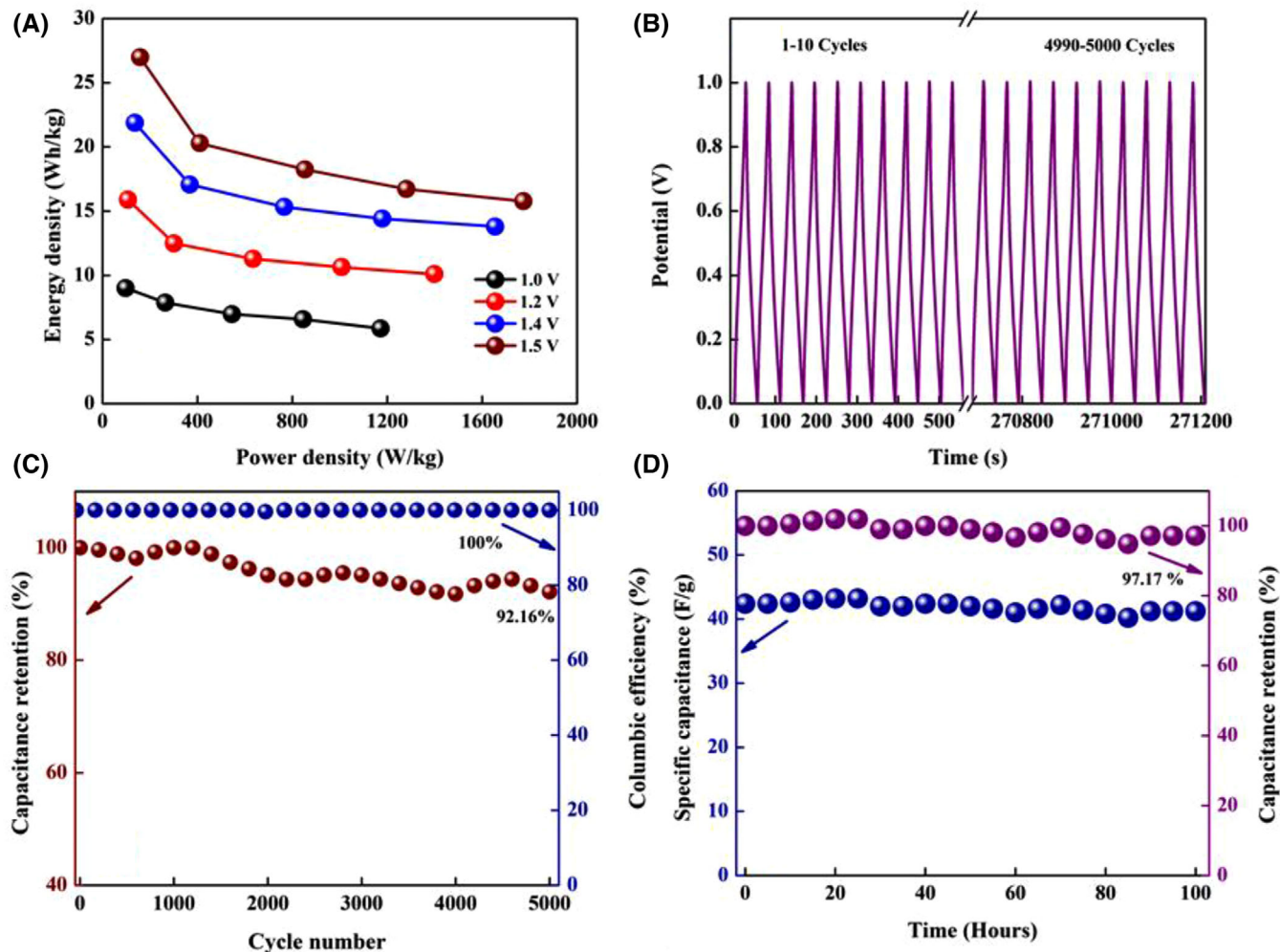


FIGURE 12 (A) Ragone plot, (B) 5000 charge discharge cycles at 1.0 A g^{-1} , (C) Efficiency and capacitance retention as a function of cycle number, (D) Floating method, capacitance and capacitance retention as a function of float time (100 hours).

Applicability of CA8 in real device depends upon satisfying some key parameters. A key performance indicator, energy density and power density of the nanocarbons, CA8 supercapacitor cell were calculated using following equations^[51]:

$$E \left(\frac{\text{Wh}}{\text{kg}} \right) = \frac{C_{\text{sp}} \times \Delta V^2}{7.2} \quad (5)$$

$$P \left(\frac{\text{W}}{\text{kg}} \right) = \frac{E \times 3600}{t} \quad (6)$$

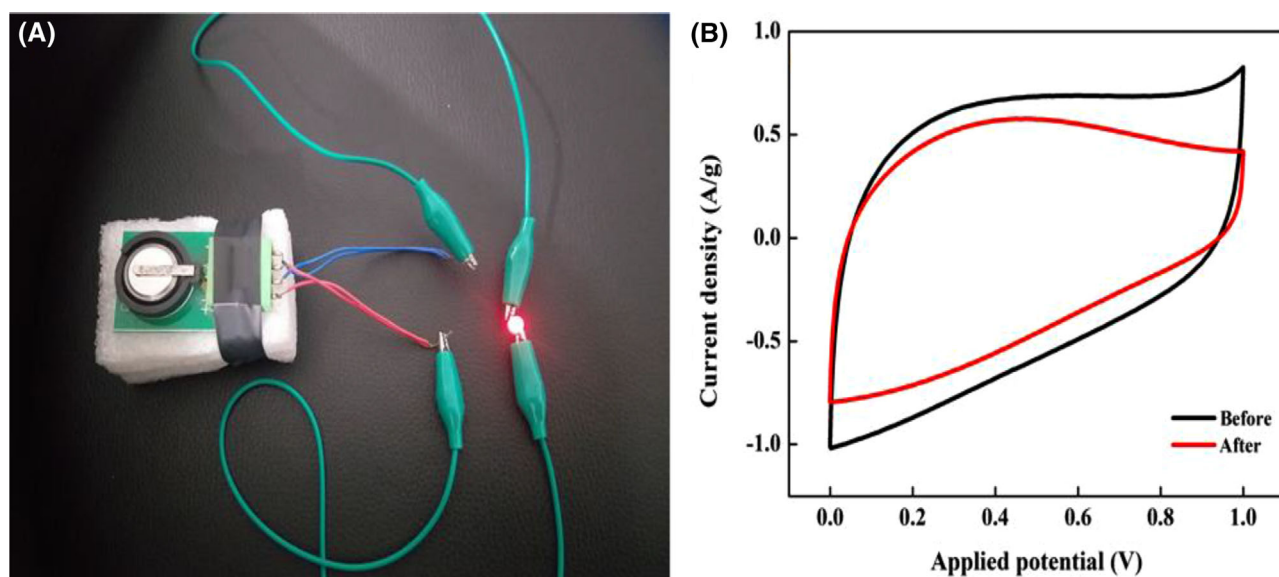
Where, C_{sp} (F/g) is the specific capacitance, ΔV (V) is the potential window and t (s) is the discharge time from the charge discharge measurements. Ragone plot depicting variation of energy density with power density is plotted as shown in Figure 12A. Maximum energy density of 27.0 Wh kg^{-1} is reached at power density of 158.79 W

kg^{-1} at 1.5 V potential. The energy density and power density being inversely related, as power density increases, energy density decreases. At high power density of 1773 W kg^{-1} , energy density could still be reached to 15.76 Wh kg^{-1} . The obtained energy parameters are better than some of the earlier reported biomass-derived carbon-based symmetrical cells in aqueous electrolyte.^[52-54] Few other earlier reported works compared with the present work is tabulated in Table 6. The cycling stability is a quintessential factor for supercapacitor electrodes. To affirm CA8 for use in practical supercapacitors, stability studies were made using galvanostatic charge discharge cycling at a current density of 1.0 A g^{-1} for 5000 cycles as shown in Figure 12B.

The CA8 coin cell symmetric supercapacitor exhibited excellent capacitance retention with more than 92% retention at the end of 5000th charge/discharge cycles, as shown in Figure 12C, indicating very good cycling ability. CA8 also exhibited seamless columbic efficiency of

TABLE 6 Performance comparison of various biomass derived carbon in two electrode setups with this work

Precursor	Potential (V)	Capacitance (F g^{-1})	Scan rate	Electrolyte	Energy density (Wh kg^{-1})	Ref.
Bamboo	3.5	146	0.2 A g^{-1}	EMIMTFSI	6.1	[55]
Pine cone	1.6	69	0.5 A g^{-1}	Gel electrolyte	24.6	[14]
Lablab purpureus	1.5	125	0.5 A g^{-1}	5 M KOH	17.9	[44]
Soybean curd residue	-	215	0.5 A g^{-1}	2 M KOH	9.95	[56]
Activated Carbon/ MnO_2	1.8	27.3	1 mV s^{-1}	1 M Na_2SO_4	9.4	[57]
Saw dust	1.0	225	0.5 A g^{-1}	6 M KOH	7.8	[58]
Rubber wood	1.0	138	0.01 A cm^{-2}	H_2SO_4	2.63	[59]
Sugarcane bagasse	1.0	225	5 mV s^{-1}	1 M H_2SO_4	7	[60]
<i>Callerya atropurpurea</i> pods	1.5	86.38	0.1 A g^{-1}	1 M KOH	27.0	This work

**FIGURE 13** (A) A single CA8 cell is Glowing of a red LED when connected to a single CA8 cell. (B) Cyclic voltammetric curves before and after 5000 cycles at 50 mV s^{-1} scan rate.

100% even after 5000 cycles owing to porous nature of CA8 facilitating effective accessibility of electrolyte ions, demonstrating excellent cycle stability and efficiency. The stability of the device was also put to test by floating method (Aging) as shown in Figure 12D. The voltage-holding curve at 1.0 A g^{-1} for a period of 100 hours, which showed 97.17% capacitance retention throughout aging time, signifying that, the cell exhibited remarkable stability throughout. A single CA8 symmetric coin cell charged for 30 seconds, when connected to a red LED, it glowed for 3.2 minutes (Figure 13A). Electrochemical performance of the device after 5000 charge discharge cycles showed minimal devaluation signifying excellent tenacity of CA8. The magnitude of attenuation of I-V response is depicted by the CV plot in Figure 13B, before and after stability studies,

which shows only minimal decrease of current in response to applied potential. The R_{CT} value is increased from 0.211 to 0.438Ω as shown in Table 4.

There is a possibility to further tune the materials in terms of functionalization, activation and also by different electrolytes and electrolyte concentrations. Studies concerning these aspects is in progress and will be reported elsewhere.

3 | CONCLUSIONS

A correlation between surface area and specific capacitance was found crucial for the fabrication of energy storage devices. The obtained capacitance for

different CA materials effectively annotates the crucial role played by the ultra micropores ($d < 0.7$ nm) for charging electrochemical double layer. Optimal dispersion of mesopores and supermicropores ($0.7 < d < 2$ nm) in CA8 elucidate the importance of channels and interconnections in pores. Such bimodal porosity is ideal as the energy storage occurs predominately in the micropores while the larger mesopores provide nimble mass-transport of electrolytes to and from the micropores. CA8 with high BET SSA of $1241 \text{ m}^2 \text{ g}^{-1}$ was tested as active electrode material for supercapacitor. The electrochemical characterization of the novel materials as supercapacitor electrode showed a specific capacitance of 326.54 F g^{-1} at 0.25 A g^{-1} . A symmetric supercapacitor cell showed a specific capacitance of 86.38 F g^{-1} at 0.1 A g^{-1} , high energy density of 27.0 Wh kg^{-1} . This symmetric supercapacitor also exhibited outstanding capacitance retention of 92.16% for 5000 charge discharge cycles and also stability of 97.17%, after voltage holding at the maximum voltage for 100 hours, suggesting that the symmetric device based on synthesized nanocarbons has a huge capacity for a high-performance electrode in electrochemical applications. The single cell of CA8 was used to glow the red LED for 3.2 minutes. The work demonstrated charge storage in micropores with low cost synthesized nanocarbons for supercapacitor applications. These findings should enable fabricating and designing of application-oriented supercapacitors: narrow pores should prove optimal for prolonged discharge duration where high energy density is desired, as in hybrid electric vehicles. For pulsed power applications, increasing the pore size might be useful. To further improve both energy density and power density, modulating the porosity and designing the carbon materials with a large volume of narrow but short pores may be beneficial along with choice of newer novel electrolytes.

4 | EXPERIMENTAL

4.1 | Synthesis and characterization of nanocarbons

The CA pods were used as raw material for the synthesis of nanocarbons. The procedure for synthesis had been discussed in detail in our previous works.^[12,40,44,61] The precursor material was ground into fine powder and subjected to one-step pyrolysis for an hour in the absence of air. Pyrolysis was conducted at different temperatures, such as 400, 600, 800, and 1000°C , the corresponding products formed would be addressed as CA4, CA6, CA8, and CA10 respectively. The carbonized products were collected, washed and dried for application studies.

The images of the particles were observed, using a TEM, on JEM 2010 (JOEL, Japan). The morphology of the particles was observed, with the aid of a FESEM, coupled to an EDS, on a SEM microscope, Apreo, FEI (Czech Republic), with a EDS machine (X Max 80, Oxford Instrument, United Kingdom). XRD was obtained from an Empyrean XRD diffractometer (Empyrean, Netherlands), for $2(\theta)$ from 10 – 80° using $\text{Cu K}\alpha$ with a radiation wavelength of 0.154 nm and a scan speed of 70.2 seconds. Raman spectra of the nanoparticles were obtained from a Raman microscope spectrometer, (RAMANforce, Nanophoton, Japan), particles diameters and zeta potential was acquired on Brookhaven NanoBrooks zetaPALS (Brookhaven, instrument, USA), surface area and porosity was obtained on a BET analyzer (ASAP2460, Micromeritics, USA), using an in-house developed method (W1-RES-BET-6P-001), by a Static volumetric N_2 gas adsorption technique, Fourier transform infrared spectroscopy (FTIR), was acquired on a Perkin Elmer spectrum BX, from 400 – 4000 cm^{-1} , using the KBr method, thermal stability of the synthesized carbon nanosphere was taken (Thermal gravimetric analysis (TGA) on a TGA7, (Perkin Elmer, USA), by heating from 50 – 1000°C at $10.0^\circ\text{C min}^{-1}$ under N_2 atmosphere.

4.2 | Electrode fabrication and electrochemical measurements

The electrodes were prepared by coating the slurry of nanocarbons, carbon black and polyvinylidene difluoride (PVDF) in 90%, 5%, and 5% ratio respectively in N-methyl-2-pyrrolidone (NMP) on nickel foam substrate. The electrochemical studies were performed in 1.0 M KOH electrolyte using three-electrode system. Platinum rod was employed as counter electrode and saturated calomel electrode was used as reference electrode. The experiments were done in AUTOLAB M204 fitted with frequency response analyzer. Cyclic voltammetry experiments for three electrode system were conducted in the potential window of -1 to 0 V at different scan rate ranging from 10 mV s^{-1} to 100 mV s^{-1} . Constant current charge discharge tests were conducted at varying current densities from 0.1 A g^{-1} to 1.0 A g^{-1} . Impedance of the system was analyzed from 100 kHz to 0.01 Hz , at 10 mV with AC current amplitude signal at open circuit potential. A practical symmetrical supercapacitor was constructed using CA8 coated on the both the electrodes isolating them from each other by a porous Whatman® glass microfiber filter membrane which was soaked in 1.0 M KOH electrolyte solution before use. This was sandwiched and pressed (at 1000 psi) into a coin cell (CR2032). Electrochemical studies were

carried out similar to the three-electrode setup under the same experimental parameters.


CONFLICT OF INTEREST

There is no conflict of interest

ACKNOWLEDGMENT

Dr. Gurumurthy Hegde would like to thank AISTDF for providing ASEAN-Indian collaborative research project, with file number, IMRC/AISTDF/CRD/2018/000019 for funding this work.

ORCID

Gurumurthy Hegde  <https://orcid.org/0000-0002-1200-5664>

REFERENCES

1. M.-M. Titirici, R. J. White, C. Falco, M. Sevilla, *Energy Environ. Sci.* **2012**, 5, 6796.
2. S. Zhang, N. Pan, *Adv. Energy Mater.* **2015**, 5, 1401401.
3. Y. Gogotsi, P. Simon, **2011**, 334, 917.
4. D. A. G. Hegde, *RSC Adv.* **2015**, 5, 88339.
5. A. Nieto-Márquez, R. Romero, A. Romero, J. L. Valverde, *J. Mater. Chem.* **2011**, 21, 1664.
6. J. Deng, M. Li, Y. Wang, *J. Green Chemistry* **2016**, 18, 4824.
7. G. Hegde, S. A. Abdul Manaf, A. Kumar, G. A. M. Ali, K. F. Chong, Z. Ngaini, K. V. Sharma, *ACS Sustainable Chem. Eng.* **2015**, 3, 2247.
8. A. Kumar, G. Hegde, S. A. B. A. Manaf, Z. Ngaini, K. V. Sharma, *Chem. Commun.* **2014**, 50, 12702.
9. N. Sudhan, K. Subramani, M. Karnan, N. Ilayaraja, M. Sathish, *Energy Fuels* **2017**, 31, 977.
10. C. Vix-Guterl, E. Frackowiak, K. Jurewicz, M. Friebe, J. Parmentier, F. Béguin, *Carbon* **2005**, 43, 1293.
11. J. Yan, A. Wang, D.-P. Kim, *J. Phys. Chem. B* **2006**, 110, 5429.
12. G. A. M. Ali, S. Supriya, K. F. Chong, E. R. Shaaban, H. Algarni, T. Maiyalagan, G. Hegde, *Biomass Convers. Biorefin.* **2019**, <https://doi.org/10.1007/s13399-019-00520-3>.
13. A. K. B., V. S. Bhat, A. Varghese, L. George, G. Hegde, **2019**, 166, B1097.
14. F. Barzegar, A. Bello, J. K. Dangbegnon, N. Manyala, X. Xia, *Appl. Energy* **2017**, 207, 417.
15. L. Borchardt, M. Oschatz, S. Kaskel, *Mater. Horiz.* **2014**, 1, 157.
16. L. Borchardt, Q.-L. Zhu, M. E. Casco, R. Berger, X. Zhuang, S. Kaskel, X. Feng, Q. Xu, *Mater. Today* **2017**, 20, 592.
17. Y. Li, D. Zhang, Y. Zhang, J. He, Y. Wang, K. Wang, Y. Xu, H. Li, Y. Wang, *J. Power Sources* **2020**, 448, 227396.
18. J. Landers, G. Y. Gor, A. V. Neimark, *Colloids Surf. A* **2013**, 437, 3.
19. Y. Sun, J. Xue, S. Dong, Y. Zhang, Y. An, B. Ding, T. Zhang, H. Dou, X. Zhang, *J. Mater. Sci.* **2020**, 55, 5166.
20. M. M. Titirici, A. Thomas, S.-H. Yu, J.-O. Müller, M. Antonietti, *Chem. Mater.* **2007**, 19, 4205.
21. V. Veeramani, M. Sivakumar, S.-M. Chen, R. Madhu, H. R. Alamri, Z. A. Allothman, M. S. A. Hossain, C.-K. Chen, Y. Yamauchi, N. Miyamoto, K. C. W. Wu, *RSC Adv.* **2017**, 7, 45668.
22. Y. Wan, Y. Shi, D. Zhao, *Chem. Mater.* **2008**, 20, 932.
23. W. Xin, Y. Song, *RSC Adv.* **2015**, 5, 83239.
24. Z. Xun, Y. Liu, J. Gu, L. Liu, P. Huo, *J. Electrochem. Soc.* **2019**, 166, A2300.
25. Y. Zhai, Y. Dou, D. Zhao, P. F. Fulvio, R. T. Mayes, S. Dai, *Adv. Mater.* **2011**, 23, 4828.
26. S. Supriya, G. Sriram, Z. Ngaini, C. Kavitha, M. Kurkuri, I. P. De Padova, G. Hegde, *Waste Biomass Valorization* **2019**, <https://doi.org/10.1007/s12649-019-00675-0>.
27. H. Yang, R. Yan, H. Chen, C. Zheng, D. H. Lee, D. T. Liang, *Energy Fuels* **2006**, 20, 388.
28. M. R. Snowdon, A. K. Mohanty, M. Misra, *ACS Sustainable Chem. Eng.* **2014**, 2, 1257.
29. Z. Xing, Z. Ju, Y. Zhao, J. Wan, Y. Zhu, Y. Qiang, Y. Qian, *Sci. Rep.* **2016**, 6, 26146.
30. G. Ma, K. Huang, Q. Zhuang, Z. Ju, *Mater. Lett.* **2016**, 174, 221.
31. J. Ou, Y. Zhang, L. Chen, Q. Zhao, Y. Meng, Y. Guo, D. Xiao, *J. Mater. Chem. A* **2015**, 3, 6534.
32. S. W. Knipe, J. R. Mycroft, A. R. Pratt, H. W. Nesbitt, G. M. Bancroft, *Geochim. Cosmochim. Acta* **1995**, 59, 1079.
33. J. Zhao, H. Lai, Z. Lyu, Y. Jiang, K. Xie, X. Wang, Q. Wu, L. Yang, Z. Jin, Y. Ma, J. Liu, Z. Hu, *Adv. Mater.* **2015**, 27, 3541.
34. G. Wang, H. Wang, X. Lu, Y. Ling, M. Yu, T. Zhai, Y. Tong, Y. Li, *Adv. Mater.* **2014**, 26, 2676.
35. D. Dollimore, G. R. Heal, *Journal of Applied Chemistry* **1964**, 14, 109.
36. J. J. Beaudoin, J. Marchand, in *Handbook of Analytical Techniques in Concrete Science and Technology* (Eds. V. S. Ramachandran, J. J. Beaudoin), William Andrew Publishing, Norwich, NY, **2001**, pp. 528-628.
37. W. Yang, L. Hou, X. Xu, Z. Li, X. Ma, F. Yang, Y. Li, *Carbon* **2018**, 130, 325.
38. Q. Chen, X. Tan, Y. Liu, S. Liu, M. Li, Y. Gu, P. Zhang, S. Ye, Z. Yang, Y. Yang, *J. Mater. Chem. A* **2020**, 8, 5773.
39. C. Zequine, C. K. Ranaweera, Z. Wang, P. R. Dvornic, P. K. Kahol, S. Singh, P. Tripathi, O. N. Srivastava, S. Singh, B. K. Gupta, G. Gupta, R. K. Gupta, *Sci. Rep.* **2017**, 7, 1174.
40. G. A. M. Ali, S. A. A. Manaf, D. A., K. F. Chong, G. Hegde, *J. Energy Chem.* **2016**, 25, 734.
41. H. Wang, Z. Li, J. K. Tak, C. M. B. Holt, X. Tan, Z. Xu, B. S. Amirkhiz, D. Harfield, A. Anyia, T. Stephenson, D. Mitlin, *Carbon* **2013**, 57, 317.
42. T. Purkait, G. Singh, D. Kumar, M. Singh, R. S. Dey, *Sci. Rep.* **2018**, 8, 640.
43. G. A. M. Ali, M. M. Yusoff, E. R. Shaaban, K. F. Chong, *Ceram. Int.* **2017**, 43, 8440.
44. G. A. M. Ali, A. Divyashree, S. Supriya, K. F. Chong, A. S. Ethiraj, M. V. Reddy, H. Algarni, G. Hegde, *Dalton Trans.* **2017**, 46, 14034.
45. J. Chmiola, G. Yushin, R. Dash, Y. Gogotsi, *J. Power Sources* **2006**, 158, 765.
46. J. Chmiola, G. Yushin, Y. Gogotsi, C. Portet, P. Simon, P. L. Taberna, *Science* **2006**, 313, 1760.
47. C. Largeot, C. Portet, J. Chmiola, P.-L. Taberna, Y. Gogotsi, P. Simon, *J. Am. Chem. Soc.* **2008**, 130, 2730.
48. C. Lastoskie, K. E. Gubbins, N. Quirke, *J. Phys. Chem.* **1993**, 97, 4786.
49. H. Shi, *Electrochim. Acta* **1996**, 41, 1633.
50. Z. Li, L. Zhang, B. S. Amirkhiz, X. Tan, Z. Xu, H. Wang, B. C. Olsen, C. M. B. Holt, D. Mitlin, *Adv. Energy Mater.* **2012**, 2, 431.

51. C. Zequine, C. K. Ranaweera, Z. Wang, S. Singh, P. Tripathi, O. N. Srivastava, B. K. Gupta, K. Ramasamy, P. K. Kahol, P. R. Dvornic, R. K. Gupta, *Sci. Rep.* **2016**, 6, 31704.
52. Q. Liang, L. Ye, Z.-H. Huang, Q. Xu, Y. Bai, F. Kang, Q.-H. Yang, *Nanoscale* **2014**, 6, 13831.
53. F. Gao, J. Qu, Z. Zhao, Z. Wang, J. Qiu, *Electrochim. Acta* **2016**, 190, 1134.
54. F. Ma, J. Wan, G. Wu, H. Zhao, *RSC Adv.* **2015**, 5, 44416.
55. Y. J. Kim, Y. Horie, S. Ozaki, Y. Matsuzawa, H. Suezaki, C. Kim, N. Miyashita, M. Endo, *Carbon* **2004**, 42, 1491.
56. G. Ma, F. Ran, H. Peng, K. Sun, Z. Zhang, Q. Yang, Z. Lei, *RSC Adv.* **2015**, 5, 83129.
57. H. Liu, K. Zhao, *J. Mater. Sci.* **2016**, 51, 9306.
58. Y. Huang, L. Peng, Y. Liu, G. Zhao, J. Y. Chen, G. Yu, *ACS Appl. Mater. Interfaces* **2016**, 8, 15205.
59. E. Taer, M. Deraman, I. Talib, A. Awitdrus, S. Hashmi, A. Umar, *Int. J. Electrochem. Sci* **2011**, 6, 3301.
60. M. Wahid, D. Puthusseri, D. Phase, S. Ogale, *Energy Fuels* **2014**, 28, 4233.
61. G. A. M. Ali, S. A. B. A. Manaf, A. Kumar, K. F. Chong, G. Hegde, *J. Phys. D: Appl. Phys.* **2014**, 47, 495307.

SUPPORTING INFORMATION

Additional supporting information may be found online in the Supporting Information section at the end of the article.

How to cite this article: Bhat VS, S S, Jayeoye TJ, et al. Influence of surface properties on electro-chemical supercapacitors utilizing *Callerya atropurpurea* pod derived porous nanocarbons: Structure property relationship between porous structures to energy storage devices. *Nano Select.* 2020;1–18. <https://doi.org/10.1002/nano.202000013>